

# Spatial control of carrier capture in two-dimensional materials: Beyond energy selection rules

Roberto Rosati,<sup>1</sup> Frank Lengers,<sup>1</sup> Doris E. Reiter,<sup>1,2</sup> and Tilmann Kuhn<sup>1,2</sup>

<sup>1</sup>*Institut für Festkörperteorie, Universität Münster,  
Wilhelm-Klemm-Str. 10, 48149 Münster, Germany*

<sup>2</sup>*Center for Multiscale Theory and Computation (CMTC), Universität Münster, 48149 Münster, Germany*

Transition metal dichalcogenide monolayers have attracted wide attention due to their remarkable optical, electronic and mechanical properties. In these materials local strain distributions effectively form quasi zero-dimensional potentials, whose localized states may be populated by carrier capture from the continuum states. Using a recently developed Lindblad single-particle approach, here we study the phonon-induced carrier capture in a MoSe<sub>2</sub> monolayer. Although one decisive control parameter is the energy selection rule, which links the energy of the incoming carriers to that of the final state via the emitted phonon, we show that additionally the spatio-temporal dynamics plays a crucial role. By varying the direction of the incoming carriers with respect to the orientation of the localized potential, we introduce a new control mechanism for the carrier capture: the spatial control.

## I. INTRODUCTION

Monolayers of a transition metal dichalcogenide (TMDC) constitute a new class of 2D materials which can be direct band gap semiconductors even if their bi- or multilayer counterparts can have an indirect gap [1–4]. This makes these material systems attractive candidates for optical and optoelectronic applications. In the TMDC monolayer localized quasi zero-dimensional (0D) confinement potentials can be effectively formed by strain tuning [5, 6], resulting in the formation of single photon emitters [7–11]. To populate such a TMDC quantum dot (QD) the phonon-induced carrier capture from the extended 2D monolayer states into the 0D QD states could be exploited. Since controlling and manipulating carriers in 0D structures is a fundamental requirement for applications, e.g., in the field of quantum information processing, the carrier capture has been studied in several semiconductor devices (with both two- [12–18] or one-dimensional [19–21] embedding materials) and by modeling on various theoretical levels, ranging from rate equations to fully quantum kinetic treatments [13, 15, 22–27]. Here we will focus on the capture from 2D into 0D states in a TMDC monolayer.

For an efficient carrier capture, having in mind Fermi's golden rule for the scattering rates, one might first think of energy selection rules. For example, if the carrier capture takes place by emission of a phonon, for an efficient capture the excess energy of the carriers in the 2D system should be one phonon energy above the energy of the discrete state in the QD. The capture rate should then be proportional to the squared transition matrix element between the delocalized initial state and the localized final state. But this simple picture neglects crucial aspects of the carrier capture on the nanometer scale. First and foremost, since the electron-phonon interaction is a local interaction, the carrier capture happens *locally*, i.e., it should take place only when the carriers are close to QD. Using a simple rate between the delocalized and local-

ized states would instantaneously reduce the density in the whole 2D material and not only close to the QD. This locality is well reproduced by approaches which fully take into account the off-diagonal nature of the electron density matrix [28–30]. The local nature, on the other hand, opens up the possibility to control the capture process beyond the energy selection rules. Employing a recently established Lindblad single-particle (LSP) approach [30] for the electron density matrix, which combines the ability to correctly treat the locality of scattering processes and the presence of quantum superposition states with a high numerical efficiency, we will show that by manipulating only the spatial configuration of the initial structure, without modifying its energetic characteristics, the spatio-temporal dynamics of the capture process can be modified in a wide range.

To be specific, we study the dynamics of an electronic wave packet traveling in a TMDC monolayer, which impinges on a localized potential forming an asymmetric QD. We particularly focus on the spatially resolved dynamics in contrast to the relaxation dynamics of the state population. We show that the capture process into the localized states of the QD depends sensitively on the geometry of the problem, in particular, when the QD is rotated with respect to the wave front of the incoming packet. This opens up the possibility for a *spatial control*. We demonstrate spatial control of the occupations of the QD as well as of the coherences between the discrete levels of the QD, which result in spatial oscillations of the captured charge density. Our results highlight the importance of spatial information for designing future devices using localized potentials in TMDC monolayers.

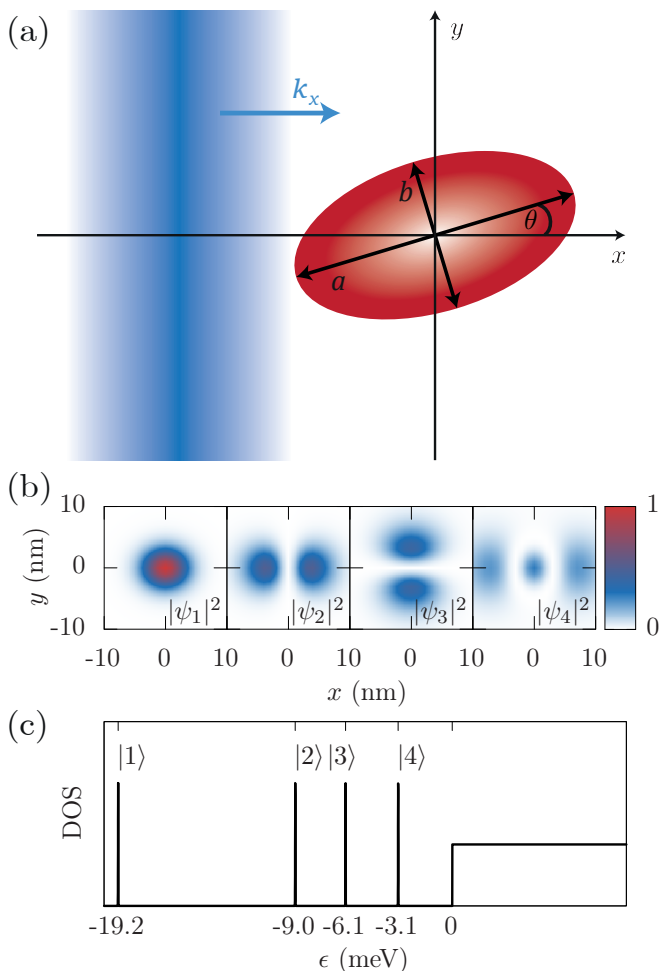


FIG. 1. (a) Sketch of the wave packet impinging on an asymmetric TMDC QD. The semiaxes of the QD are given by  $a$  (long semiaxis) and  $b$  (short semiaxis) [see Eq. (2)]. The angle  $\theta$  defines the tilt between the propagation direction of the incoming wave packet and the long axis of the QD. (b) Square moduli of the bound-states wave functions for the potential in Eq. (2) with  $\theta = 0$  and (c) corresponding density of states (DOS) of the conduction band showing the energies of the four bound states with  $\epsilon < 0$ .

## II. THEORETICAL BACKGROUND

### A. System set-up

For our studies we consider an electronic wave packet traveling in a TMDC monolayer impinging on a QD potential as sketched in Fig. 1(a). Carriers can be captured inside the potential by the emission of a longitudinal optical (LO) phonon with energy  $E_{LO}$ , as will be described in Sec. II B.

For the description of the states we will use the envelope function formalism, in which the states  $|\alpha\rangle$  corresponding to the wave functions  $\psi_\alpha(\mathbf{r})$  are obtained by solving the Schrödinger equation

$$[H_{\text{TMDC}} + V(\mathbf{r})]\psi_\alpha(\mathbf{r}) = \epsilon_\alpha\psi_\alpha(\mathbf{r}), \quad (1)$$

where  $\mathbf{r}$  is the 2D position vector in the  $xy$ -plane,  $H_{\text{TMDC}}$  is the Hamiltonian of the TMDC lattice and  $V(\mathbf{r})$  the QD potential. For the confinement potential we assume an elliptically shaped QD with long semiaxis  $a$  and short semiaxis  $b$ , as sketched in Fig. 1(a), which we model by

$$V(\mathbf{r}) = -V_0 \text{sech} \left( \sqrt{\frac{x'(\theta)^2}{a^2} + \frac{y'(\theta)^2}{b^2}} \right), \quad (2)$$

where  $\text{sech}$  is the hyperbolic secant and

$$\begin{pmatrix} x'(\theta) \\ y'(\theta) \end{pmatrix} = \begin{pmatrix} \cos(\theta) & \sin(\theta) \\ -\sin(\theta) & \cos(\theta) \end{pmatrix} \begin{pmatrix} x \\ y \end{pmatrix}. \quad (3)$$

According to Eq. (3), the long axis of the QD is tilted by the angle  $\theta$  with respect to the  $x$ -axis.

We restrict ourselves here to a single electronic subband. Details on the TMDC model used in  $H_{\text{TMDC}}$  can be found in the appendix A. The solutions of the Schrödinger equation are composed of continuum states with energies above the band gap and delocalized over the 2D monolayer, and of  $n_b$  bound states ( $\alpha = 1, \dots, n_b$ ), which are spatially localized in the QD region and have a discrete energy spectrum below the TMDC band minimum.

As a material for our simulations we choose MoSe<sub>2</sub> with the material parameters given in appendix C. For the QD we set  $b = 3$  nm,  $a = \sqrt{2}b = 4.2$  nm and  $V_0 = 35$  meV, while  $\theta$  is a variable tilt angle. With these parameters the QD has  $n_b = 4$  bound states at energies  $\epsilon_i$  lying  $-19.2, -9.0, -6.1$  and  $-3.1$  meV below the bottom of the conduction band of the 2D material. The square moduli of the wave functions of the bound states are depicted in Fig. 1(b) for the case of  $\theta = 0$ , i.e., for a QD elongated along the  $x$ -direction. State  $|1\rangle$  is the ground state with even parity and a weak elongation along  $x$ . The excited states  $|2\rangle$  and  $|3\rangle$  have an odd-parity and are elongated along the long and short axes of the QD, respectively, which for  $\theta = 0$  coincide with the  $x$ - and  $y$ -directions. State  $|4\rangle$  has again even parity and is elongated along the long axis. The corresponding density of states (DOS) of the structure is schematically shown in Fig. 1(c).

The initial wave packet is chosen to be of wave-front type, which in the basis of the free TMDC states can be written as

$$\begin{aligned} \rho_{\mathbf{k} + \frac{\mathbf{k}'}{2}, \mathbf{k} - \frac{\mathbf{k}'}{2}}^\circ &\propto e^{-\frac{1}{2}(k'_x \Delta_x)^2} e^{-i k'_x x_0} e^{-\left(\frac{(\hbar^2 k_y^2)/(2m^*) - E_0}{\sqrt{2}\Delta_E}\right)^2} \\ &\times \theta(k_x) \delta(k'_y) \delta(k_y), \end{aligned} \quad (4)$$

where  $\mathbf{k} = (k_x, k_y)$  is a 2D wave vector and  $\theta(k_x)$  is the Heaviside step function. The wave packet has a finite width in space determined by  $\Delta_x = 10$  nm and in energy given by  $\Delta_E = 5$  meV. It is centered at  $x_0 = -70$  nm, i.e., sufficiently far from the QD such that initially there is no overlap with the QD. The excess energy, which determines the velocity of the wave packet, is taken to be  $E_0 = 26.8$  meV  $\approx (\epsilon_2 + \epsilon_3)/2 + E_{LO}$ , such that from an

energetic point of view the capture into the states  $|2\rangle$  and  $|3\rangle$  should be equally probable.

We emphasize that the key parameter in our study will be the relative orientation of the wave-packet propagation direction with respect to the orientation of the elongated QD. Because we fix the propagation direction to the  $x$ -direction, the relative orientation is quantified by the tilt angle  $\theta$  of the potential as introduced in Eq. (2).

## B. Description of the dynamics

To describe the dynamics of the wave packet we set up the equation of motion for the density matrix  $\rho_{\alpha\alpha'}$ , which in general can be written as [31–35]

$$\frac{d\rho_{\alpha\alpha'}}{dt} = \frac{d\rho_{\alpha\alpha'}}{dt}\Big|_{\text{free}} + \frac{d\rho_{\alpha\alpha'}}{dt}\Big|_{\text{scat}}, \quad (5)$$

where  $d\rho_{\alpha\alpha'}/dt|_{\text{free}} = -i(\epsilon_{\alpha} - \epsilon_{\alpha'})\rho_{\alpha\alpha'}/\hbar$  gives the scattering-free contributions, while  $d\rho_{\alpha\alpha'}/dt|_{\text{scat}}$  describes the scattering.

The initial wave packet [cf. Eq. (4)] corresponds to an excitation of only continuum states, from which a charge transfer into the bound states may take place by scattering mechanisms. In view of the initial conditions considered here, we will concentrate on the carrier capture by emission of intravalley LO optical phonon modes, whose Fröhlich interaction induces scattering coefficients  $g_{\mathbf{q}}$  between states  $|\mathbf{k} + \mathbf{q}\rangle$  and  $|\mathbf{k}\rangle$  in the form of [36, 37]

$$g_{\mathbf{q}} \equiv g_q = \frac{g_{\text{Fr}}}{\sqrt{A}} \text{erfc}(qd/2), \quad (6)$$

with  $\mathbf{q}$  being the phononic wave vector, while  $\text{erfc}(x)$  is the complementary error function and the constants  $g_{\text{Fr}}$  and  $d$  depend on the material. Other scattering mechanisms, i.e., with different phonon modes or Coulomb interaction, are not efficient here and hence disregarded, see appendix B.

In the dynamics of Eq. (5) we describe the scattering using the LSP equation which we recently developed [30] by tailoring an alternative Markov approach [31, 38], the latter already used for spatio-temporal studies in several materials [32–34]. In particular, the scattering terms can be written as

$$\frac{d\rho_{\alpha\alpha'}}{dt}\Big|_{\text{scat}} = \frac{1}{2} \sum_{\bar{\alpha}\bar{\alpha}', \mathbf{q}} (A_{\alpha\bar{\alpha}}^{\mathbf{q}} A_{\alpha'\bar{\alpha}'}^{\mathbf{q}*} \rho_{\bar{\alpha}\bar{\alpha}'} - A_{\bar{\alpha}\alpha}^{\mathbf{q}*} A_{\bar{\alpha}'\alpha'}^{\mathbf{q}} \rho_{\bar{\alpha}'\alpha'}) + \text{H.c.}, \quad (7)$$

where

$$A_{\alpha\alpha'}^{\mathbf{q}} = \sqrt{\frac{2\pi}{\hbar}} g_{\alpha\alpha'; \mathbf{q}} \frac{e^{-\left(\frac{\epsilon_{\alpha} - \epsilon_{\alpha'} + E_{\text{LO}}}{2\bar{\epsilon}}\right)^2}}{(2\pi\bar{\epsilon}^2)^{\frac{1}{4}}} \quad (8)$$

and H.c. denotes Hermitian conjugate while  $g_{\alpha\alpha'; \mathbf{q}} = \sum_{\mathbf{k}} \langle \alpha | \mathbf{k} \rangle g_{\mathbf{q}} \langle \mathbf{k} + \mathbf{q} | \alpha' \rangle$ . We set  $\bar{\epsilon} = 3.5$  meV ( $\bar{\epsilon} \rightarrow 0$ ) for the transitions into bound (continuum) states. More details on the approach, including a discussion about its ability to recover most of the features obtained in a quantum

kinetic descriptions and the meaning of  $\bar{\epsilon}$ , may be found in Ref. [30]. We stress however that the LSP equation is a Markovian treatment [31, 38], therefore it is computationally much lighter than a full quantum kinetic approach [28, 29, 35]. This computational lightness of the LSP approach has allowed us to extend previous studies, which have been mainly focused on effective 1D systems, to fully 2D systems. Nevertheless, this treatment is able to describe arbitrary spatially inhomogeneous carrier distributions and, importantly, naturally includes the possibility that the final state of a scattering process is given by a quantum-mechanical superposition state.

The spatio-temporal dynamics of electrons in the TMDC monolayer are obtained by numerically integrating the equations of motion. We remind that diagonal elements of the density matrix  $f_{\alpha} = \rho_{\alpha\alpha}$  are the *populations*, while the off-diagonal ones  $\rho_{\alpha\alpha'}$  with  $\alpha' \neq \alpha$  are the *coherences*. Outside the QD region the continuum 2D states are essentially plane waves, and the full single-electron density matrix including both diagonal and off-diagonal elements has to be taken into account for describing spatial inhomogeneities. The populations may be interpreted as distribution in energy, while the distribution in space is provided by

$$n(\mathbf{r}) = \sum_{\alpha, \alpha'} \rho_{\alpha\alpha'} \psi_{\alpha'}^*(\mathbf{r}) \psi_{\alpha}(\mathbf{r}), \quad (9)$$

where  $\alpha, \alpha'$  run over all the states (continuum and bound), thus providing the whole electronic distribution (i.e., captured or not). The spatial distribution of the trapped charge  $n_{\text{QD}}(\mathbf{r})$  is described analogously when restricting  $\alpha, \alpha'$  to the  $n_b$  bound states.

## III. RESULTS

### A. Capture dynamics

We start our analysis by discussing the spatio-temporal dynamics of the capture process. Snapshots of the spatio-temporal evolution of the wave packet without electron-phonon coupling (left column) and with electron-phonon coupling (right column) are shown in Fig. 2. The dynamics can be separated into three phases: (i) the wave packet propagation towards the QD (first row), (ii) the crossing of the wave packet over the QD (second row), and (iii) the motion of the transmitted wave packet (third row). The wave packet propagation in phase (i) is essentially the same with and without phonon interaction. At  $t = 0.3$  ps the wave front has just reached the QD and the phonon emission is not yet effective. There is only a very weak redistribution within the continuum states due to the small amount of occupation above the LO phonon energy. Already the first phase shows that the locality of the capture is well reproduced by the simulation: Without overlapping between wave packet and QD the electron-phonon interaction cannot lead to transitions from continuum into localized states. Technically

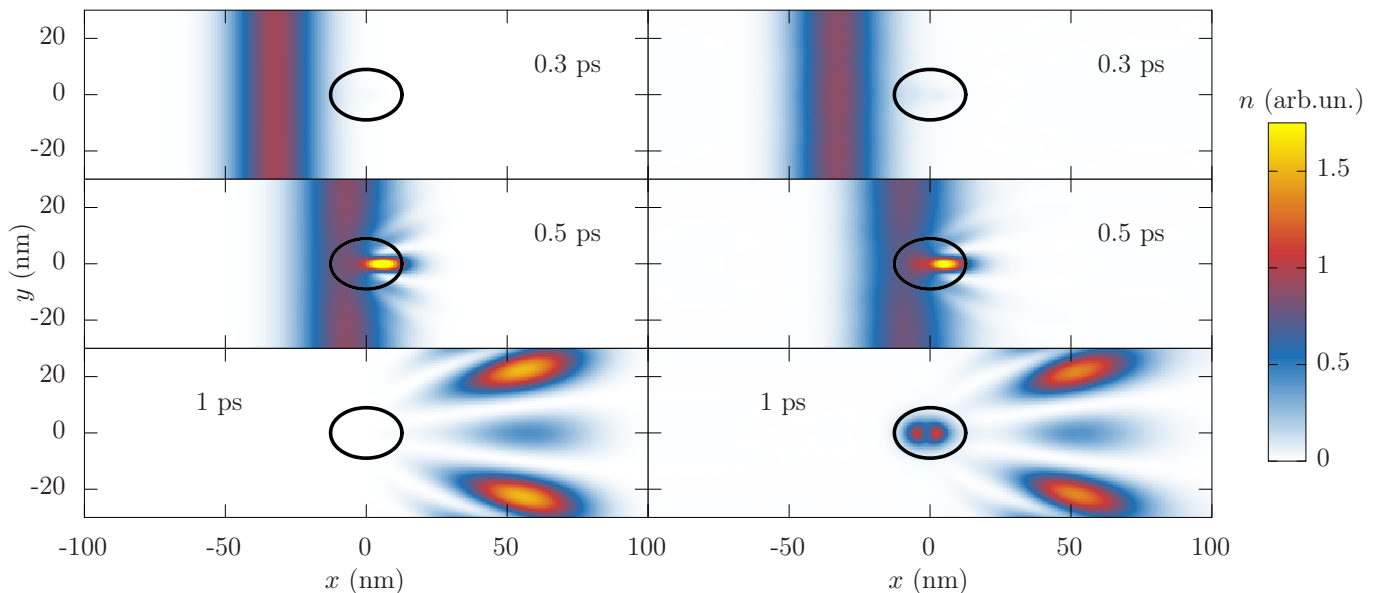


FIG. 2. Electronic density  $n(\mathbf{r})$  for the wave packet impinging on the QD for  $\theta = 0$  without (left column) and with (right column) electron-phonon coupling. The charge has been normalized to the height of the initial wave packet. The black line marks the QD region (defined as where the potential has dropped to 10% of its maximum). The three rows show snapshots of the spatio-temporal dynamics for the three phases: Propagation towards the QD at  $t = 0.3$  ps, crossing of the QD at  $t = 0.5$  ps and transmission at  $t = 1.0$  ps.

this can be traced back to a cancelation between diagonal and off-diagonal contributions in the equation of motion for the density matrix [30]

When arriving at the QD [phase (ii)], the wave front shape of the wave packet is lost and a pattern appears. Already on the scattering-free level, we note an intense peak of charge in the QD region along the  $y = 0$  line, which is strongly elongated along  $x$ . Although during phase (ii) a capture of electrons into the localized potential sets in, the density in the QD area is still rather similar with and without carrier-phonon coupling, showing that this density is still mainly associated with the continuum states and caused by their deviations from plane waves above the QD due to their orthogonality with respect to the bound states. In contrast, after the wave packet has traversed the QD [phase (iii)], an electronic density remaining in the QD area is clearly visible only in the presence of electron-phonon interaction. The fringes of the transmitted wave packet exhibit only slight quantitative modifications by the scattering processes, while their qualitative shape is preserved.

To get a more quantitative picture of the capture dynamics, we now analyze the occupations  $f_i$  of the bound states as a function of time. They are shown in Fig. 3(a) for three different orientations of the QD:  $\theta = 0$ ,  $\theta = \pi/4$  and  $\theta = \pi/2$ . For all occupations we find a similar behavior: After a certain time, the occupations rise monotonically up to their respective maximal values and subsequently stay constant. This again reflects the locality of the capture process: Only when the wave packet is in the region of the QD a capture takes place. In analogy

with the 1D case [30] we can define a scattering time which is here ranging between 300 and 400 fs, the exact value depending on the angle  $\theta$  and the state  $|i\rangle$ .

Because the energy distribution of the initial wave packet and the energies of the bound states are independent of the angle  $\theta$ , based on energy selection rules one might expect that the final occupations  $\bar{f}_i$  (i.e., the occupations  $f_i$  after the wave packet has traversed the QD) are weakly dependent of the angle  $\theta$ . In particular, the occupation of the states  $|2\rangle$  and  $|3\rangle$  should be rather similar due to the choice of excess energy of the wave packet. However, when looking at Fig. 3(a) we find pronounced differences in the occupations of these states upon variation of  $\theta$ . When comparing the final occupations for a QD elongated along the  $x$ -direction ( $\theta = 0$ , upper panel) and the  $y$ -direction ( $\theta = \pi/2$ , lower panel), we find that the occupations of the states  $|2\rangle$  and  $|3\rangle$  are inverted in the two cases: While for  $\theta = 0$  the occupation of state  $|2\rangle$  is much higher than the one of state  $|3\rangle$ , for  $\theta = \pi/2$  the occupation of state  $|3\rangle$  is higher than the one of state  $|2\rangle$ . Taking into account the spatial shape of the wave functions, we thus find that capture occurs predominantly into the state which is elongated along the propagation direction. Indeed, for  $\theta = \pi/4$ , i.e., when the QD lies diagonal with respect to the incoming wave packet, the occupations of  $|2\rangle$  and  $|3\rangle$  are almost the same (central panel). Remarkably, at  $\theta = 0$  we find that also  $\bar{f}_4$  is bigger than  $\bar{f}_3$ , despite its energetic separation from the resonant energy being much bigger than the one of state  $|3\rangle$ , suggesting a *spatial selection rule* able to go beyond the pure energetic considerations.

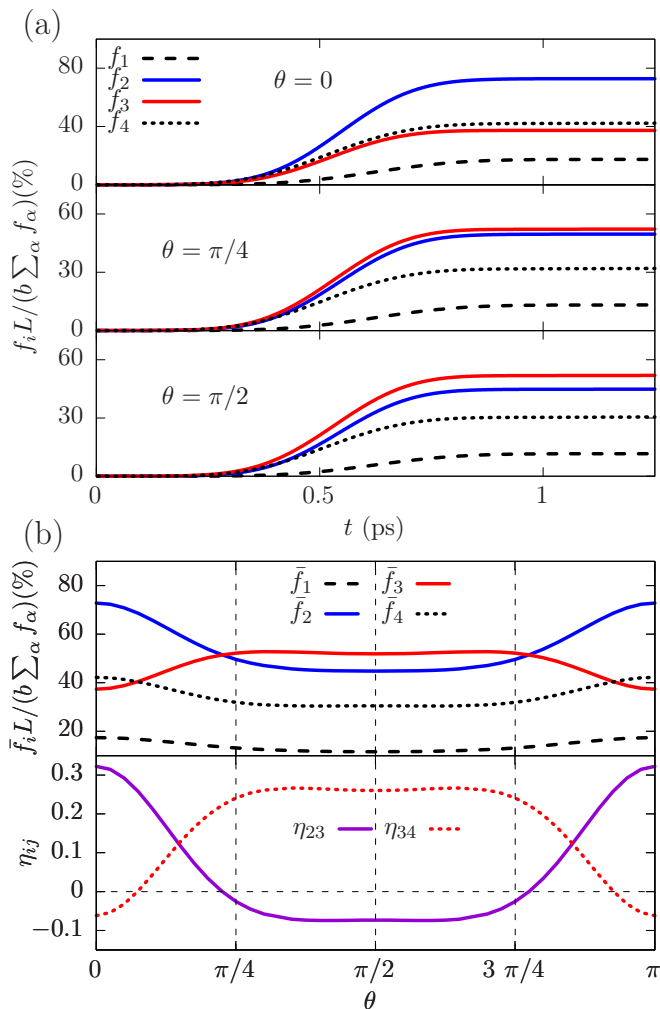


FIG. 3. (a) Evolution of the occupations of the bound states for  $\theta=0$  (top),  $\theta = \pi/4$  (center) and  $\theta = \pi/2$  (bottom). (b) Dependence of the final occupations  $\bar{f}_i$  (upper panel) and the relative occupations  $\eta_{ij}$  (lower panel) on the QD orientation  $\theta$ . All occupations are normalized to the density contained by the initial electronic distribution in a stripe of height  $b/L$ .

We quantify the orientation dependence of the captured populations in Fig. 3(b), where in the upper panel we show the final occupations  $\bar{f}_i$  as functions of the angle  $\theta$ . We find that the stationary populations corresponding to the states  $|i\rangle$  elongated along the major axis (i.e.,  $\bar{f}_1$ ,  $\bar{f}_2$  and  $\bar{f}_4$ ) decrease by rotating the QD from 0 to  $\pi/2$ , while the occupation  $\bar{f}_3$  of state  $|3\rangle$ , which is elongated along the orthogonal direction, increases. Thanks to their different spatial shapes, a rotation of the QD results in the fact that  $\bar{f}_3$  overcomes first  $\bar{f}_4$  and then  $\bar{f}_2$ : This spatial selectivity is quantified in the lower panel in terms of the relative occupations

$$\eta_{ij} = \frac{\bar{f}_i - \bar{f}_j}{\bar{f}_i + \bar{f}_j}, \quad (10)$$

where the switch in the state occupations is reflected in a change of the signs.

This  $\theta$ -dependence is the signature of a *spatial selection rule* based on the relative orientation of the propagation direction of the wave packet and the QD long axis, which complements the energy selection rule determined by the phonon energy  $E_{\text{LO}}$ . This implies that several aspects vary with the angle: the effective scattering matrix elements, which are determined by the wave packet's propagation direction, and also the overlap between receiving bound state and emitting traveling wave packet, i.e., the interplay between nontrivial spatio-temporal evolution and the locality of the carrier capture.

## B. Coherence control

The spatial control is not limited to the magnitude of the captured occupations, it further has great impact on the quantum coherences between the bound states. When the potential consists of several bound states, in general a capture into a coherent superposition of these states takes place, resulting in an oscillation of the captured density [28, 30, 39]. Such a build up of superposition states cannot be described by approaches which treat the capture only in terms of scattering rates between the different states. However, we have recently shown that the LSP approach, though being of Markovian nature, indeed adequately describes this genuine quantum mechanical capture behavior [30] because it fully includes off-diagonal elements of the electron density matrix.

We start analyzing the dynamics of the trapped density  $n_{\text{QD}}(x, y)$ , i.e., the density in the subspace of the bound states, for the three orientations discussed above: Figure 4(a) shows snapshots of this quantity, normalized as in Fig. 2, while the full time evolution is displayed in Ancillary Movie 1(a). Let us start our discussion with the cases of wave-packet propagation along the long ( $\theta = 0$ , top row) or short ( $\theta = \pi/2$ , bottom row) QD axis. In both cases we observe charge oscillations induced by the capture process along the propagation direction. These oscillations can also be seen in the top and bottom row of Fig. 4(b), where a cut through the captured density at  $y = 0$  is plotted as a function of position  $x$  and time  $t$ . The charge distributions are always symmetric with respect to  $y = 0$  and have their maximum at  $y = 0$ . This is also confirmed by looking at the time-dependence of the center of mass of the charge distribution, defined as

$$\begin{aligned} \langle r_x \rangle &= \frac{\int x n_{\text{QD}}(x, y) dx dy}{\int n_{\text{QD}}(x, y) dx dy}, \\ \langle r_y \rangle &= \frac{\int y n_{\text{QD}}(x, y) dx dy}{\int n_{\text{QD}}(x, y) dx dy}, \end{aligned} \quad (11)$$

and plotted in Fig. 4(c) [see also Ancillary Movie 1(b)]. In the top and bottom panel we find for the transverse component  $\langle r_y \rangle = 0$  at any time, while the longitudinal component  $\langle r_x \rangle$  exhibits oscillations which are roughly sinusoidal. From a closer look we can identify an oscillation period for  $\theta = 0$  with  $T_0 \approx 0.7$  ps. For  $\theta = \pi/2$  we

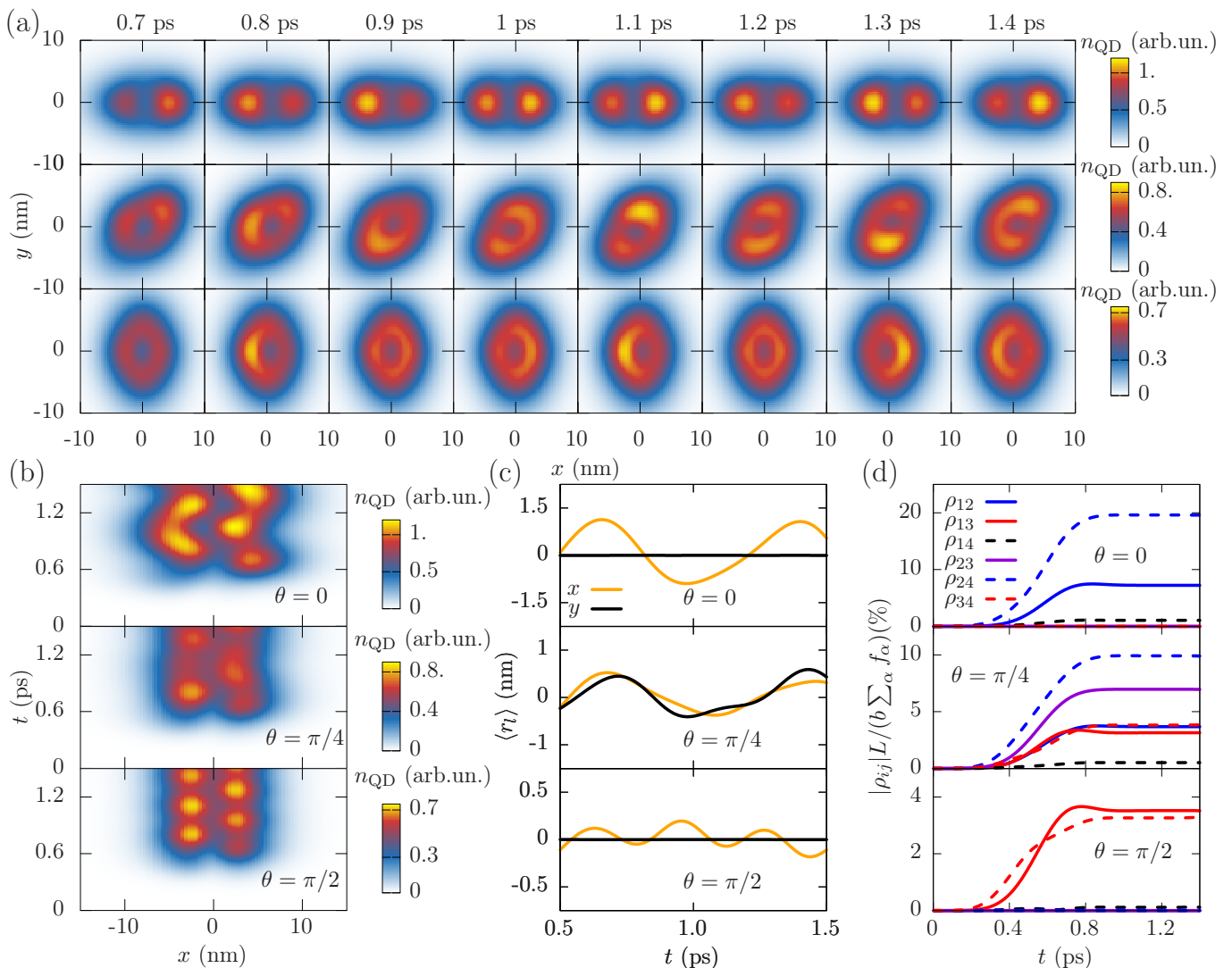


FIG. 4. (a) Snapshots of the captured charge density  $n_{\text{QD}}(\mathbf{r})$  [see Ancillary Movie 1(a) for the full time evolution]. (b) Spatio-temporal dynamics of the captured charge density along the  $x$ -axis [i.e.,  $n_{\text{QD}}(x, y = 0, t)$ ]. (c) Temporal evolution of the  $x$ - and  $y$ -components of the center of mass of the trapped charge distribution [see also Ancillary Movie 1(b)]. (d) Evolution of the normalized coherences. All figures are for the three QD orientations  $\theta = 0$  (upper row),  $\theta = \pi/4$  (central row), and  $\theta = \pi/2$  (lower row).

find the period to be  $T_{\pi/2} \approx 0.3$  ps. The time evolutions in space of the center of mass ( $\langle r_x \rangle, \langle r_y \rangle$ ) are shown in Ancillary Movie 1(b) (top and bottom row), where we see a left/right oscillatory motion.

In contrast, for a QD tilted by an angle  $\theta = \pi/4$  with respect to the propagation direction a much more complicated spatio-temporal behavior is observed [central row in Figs. 4 and Ancillary Movie 1(a)]. Now we find an oscillation that, although roughly along the long axis of the QD, is not fixed in time, which can be seen from the fact that in the central panel of Fig. 4(c) the components  $\langle r_x \rangle$  and  $\langle r_y \rangle$  are not always proportional to each other, as it would be the case for a strict oscillation along the long axis of the QD. In the center of mass motion [see central panel in Ancillary Movie 1(b)] a quasi-ergodic

motion of ( $\langle r_x \rangle, \langle r_y \rangle$ ) following the form of the potential ellipse  $V(\mathbf{r})$  is observed. Despite the complexity of the oscillations, we can still estimate the period to roughly  $T_{\pi/4} \approx 0.7$  ps.

The spatio-temporal dynamics of the captured charge density can be understood when looking at the off-diagonal elements of the density matrix  $\rho_{ij}$  in the subspace of the bound states. Their moduli  $|\rho_{ij}|$ , normalized in the same way as the diagonal elements in Fig. 3, are shown in Fig. 4(d). Like the diagonal elements they show the characteristic capture behavior: Before the wave packet has reached the QD region they are zero. Then they build up and remain constant when the wave packet has passed the QD. For the coherences the dependence on the orientation angle  $\theta$  is even more pronounced

than for the occupations. For  $\theta = 0$  (top panel) we find at any time  $\rho_{13} = \rho_{23} = \rho_{34} = 0$  while for  $\theta = \pi/2$  (bottom panel) we have  $\rho_{12} = \rho_{23} = \rho_{24} = 0$ . This reflects the symmetry of the set-up: The incoming wave packet is homogeneous in  $y$ -direction. Therefore it can never excite a superposition between a state with even and one with odd parity in  $y$ -direction. For  $\theta = 0$  state  $|3\rangle$  is the only state with odd parity in  $y$ -direction. Indeed, no coherences with this state are excited and the charge distribution keeps its mirror symmetry with respect to  $y = 0$ . Correspondingly, for  $\theta = \pi/2$  state  $|2\rangle$  is the only state with odd parity in  $y$ -direction and no coherences with this state are excited. The spatial selection rule is thus able to inhibit completely the appearance of specific coherences. When looking at the magnitude of the excited coherences, we find for  $\theta = 0$  a dominant excitation of  $\rho_{24}$ . The corresponding energy difference is  $\epsilon_4 - \epsilon_2 = 5.9$  meV giving rise to the oscillation period  $T_0 \approx 0.7$  ps. There is an additional pronounced contribution from  $\rho_{12}$  with an energy difference  $\epsilon_2 - \epsilon_1 = 10.2$  meV, from which one can identify a second period  $T \approx 0.4$  ps which leads to the fast oscillations in Fig. 4(b). For  $\theta = \pi/2$  there are two contributions of almost equal strength,  $\rho_{13}$  with an energy difference of  $\epsilon_3 - \epsilon_1 = 13.1$  meV corresponding to the period of  $T_{\pi/2} \approx 0.3$  ps and  $\rho_{34}$  with  $\epsilon_4 - \epsilon_3 = 3.0$  meV, corresponding to a period of about 1.3 ps and which gives rise to the long time modulations visible in Fig. 4(c). In both cases there is a weak excitation of the coherence  $\rho_{14}$ , which leads to a slight breathing mode contribution of the charge dynamics. This coherence is allowed for symmetry reasons but it is strongly suppressed by the weak overlap of the wave functions and the large energy difference of the states.

If the axis of the QD is tilted by  $\theta = \pi/4$  with respect to the propagation direction of the wave packet, the symmetry selection rules are relaxed because none of the bound states has a definite parity with respect to the  $y$ -axis. Therefore, all the quantum coherences can be excited and, as can be seen in the central panel of Fig. 4(d), they indeed are all excited. The strongest one is  $\rho_{24}$ , which gives rise to oscillations along the long axis with the period  $T_{\pi/4} \approx 0.7$  ps, like in the case  $\theta = 0$ . The next strongest coherence is  $\rho_{23}$ , which is neither excited for  $\theta = 0$  nor for  $\theta = \pi/2$ . This coherence induces a rotational-like oscillation in the charge density. Finally, there are almost equally strong contributions from  $\rho_{12}$ , modifying the oscillation along the long axis, as well as from  $\rho_{13}$  and  $\rho_{34}$ , introducing oscillations along the short axis. The combination of all these coherences gives rise to the complex charge dynamics.

#### IV. CONCLUSION

In this paper we have shown how in two-dimensional materials the carrier capture from a traveling electronic wave packet into localized states of an embedded quantum dot changes with the relative orientation of travel-

ing direction and quantum dot elongation, despite all the energetic parameters remain fixed. This proves the effectiveness of spatial selection rules, which are beyond the usual energetic ones and may find several applications in controlling charge carrier dynamics on the nanoscale. To be specific, we considered a monolayer of the transition metal dichalcogenide MoSe<sub>2</sub> with a localization potential as can be formed by a local strain distribution. In this material, the electrons are efficiently coupled to optical phonons, which leads to the capture of carriers into the localized states.

To model such a spatial control a theoretical approach is needed which, on the one hand, fully includes spatially inhomogeneous structures and spatially inhomogeneous carrier distributions and, on the other hand, is able to describe genuine quantum features like capture processes into coherent superposition states and the subsequent dynamics of these superpositions. For this purpose we have employed a recently developed Lindblad single particle approach in the density matrix formalism including electron-phonon scattering. A big advantage of this approach compared to, e.g., a fully quantum kinetic treatment, is its strongly reduced computational complexity, which allowed us to simulate the full 2D problem discussed here. Though treating the interaction processes on a Markovian level, this approach has been shown to well reproduce the *locality* of the scattering process, a basic ingredient to describe the spatial control employed here.

To be specific, we have considered a wave packet traveling in a MoSe<sub>2</sub> monolayer impinging on an asymmetric localized potential with bound states. The carriers can be trapped into the bound states by emission of LO phonons. We have shown that the spatial control realized by varying the angle between wave-packet propagation direction and long axis of the quantum dot affects two aspects of the carrier capture: (a) The occupations of the bound states depend sensitively on the angle and can be varied significantly by changing the orientation. This happens despite the energy selection rules do not change when varying the relative orientation. (b) The coherences between bound states, which build up during the capture process, strongly depend on the orientation. Specific coherences can be entirely switched off in the case of highly symmetric configurations of wave packet and quantum dot orientation. The capture into superpositions of the bound states is particularly visible in the spatio-temporal dynamics of the trapped density, which shows an oscillatory behavior. The period of the oscillations depends on the involved states and hence is a direct measure for the strength of the coherences. For a less symmetric situation, e.g., for a tilt angle of  $\theta = \pi/4$ , a large number of coherences may be excited by the capture process leading to a complicated spatio-temporal dynamics.

In conclusion, the locality of carrier capture is crucial for a correct description of such processes. This has allowed us to exploit a *spatial* control of carrier capture processes beyond the energy selection rules. In the

process of miniaturization, the spatio-temporal dynamics will play a more and more decisive role. In this context, our studies establish the foundations for describing and exploiting the spatial control of charge carrier dynamics in 2D systems.

## ACKNOWLEDGEMENTS

We thank Daniel Wigger for useful discussions.

## Appendix A: TMDC structure

A free-standing monolayer TMDC has a hexagonal lattice with direct band gap at  $\mathbf{K}$  and  $\mathbf{K}'$  valleys, where the Hamiltonian results in a single electron dispersion relation reading  $E_{\mathbf{k},\bar{b},\bar{s},\bar{v}} = \bar{v} \bar{s} \frac{\lambda_c + \lambda_v}{2} + a_0 t \bar{b} \sqrt{[(\Delta_G - \bar{v}\bar{s}(\lambda_v - \lambda_c))/(2a_0t)]^2 + |\mathbf{k}|^2}$ , where  $\mathbf{k}$  is a two-dimensional wave vector, the constants  $\Delta_G$ ,  $\lambda_{c/v}$ , providing respectively band gap and half conduction/valence band splitting, and the parameters  $a_0$  and  $t$  depend on the specific TMDC, while the label  $\bar{b} = \pm 1$  stands for conduction/valence band,  $\bar{s} = \pm 1$  for spin up/down and  $\bar{v} = \pm 1$  for valley  $\mathbf{K}/\mathbf{K}'$  [40–42]. Although a TMDC monolayer has an involved band structure [43–46], in view of the scales involved (see appendix B) in this work we restrict ourselves to one subband with  $\bar{b} = \bar{s} = \bar{v} = 1$  and to a region close to its minimum, where the dispersion relation is almost parabolic and the associated eigenstates may be approximated as scalar states like in conventional semiconductors,  $\psi_{\mathbf{k}}(\mathbf{r}) \equiv \langle \mathbf{r} | \mathbf{k} \rangle = e^{i\mathbf{k}\cdot\mathbf{r}}/\sqrt{A}$ , with  $A = L^2$  being the normalization area of the two-dimensional device. Note that Eq. (1) has been solved by expanding the wave functions  $\psi_{\alpha}(\mathbf{r})$  in these states  $|\mathbf{k}\rangle$  with  $\langle \mathbf{k} | H_{\text{TMDC}} | \mathbf{k}' \rangle = E_{\mathbf{k},1,1,1} \delta_{\mathbf{k},\mathbf{k}'}$ .

The excess energy  $E_0$  we chose lies just above the minimum of the subband, i.e., where the scalar parabolic approximation works more effectively and the excitonic effects should be of minor importance [47–49], in contrast to what happens far below the band gap, where the excitonic effects should be typically dominant [45, 46, 50–52].

## Appendix B: Scattering mechanisms

In view of the energetic separation between continuum and bound states we disregard the intravalley acousti-

cal phonon modes. In general, TMDCs have six optical modes, of which however only two – the so-called LO and  $A_1$  modes – are able to effectively influence the electron dynamics [53]. For MoSe<sub>2</sub> the electron-LO phonon coupling coefficients in the long wavelength limit are one order of magnitude bigger than the electron- $A_1$  phonon ones [53]; as a consequence, here we restrict ourselves to intravalley LO phonons with a fixed energy of  $E_{\text{LO}} \approx 34.4$  meV [53]. We consider the low temperature limit,  $k_B T \ll E_{\text{LO}}$  ( $T$  denoting the temperature and  $k_B$  Boltzmann’s constant), in which only (spontaneous) phonon emission processes are possible. The surrounding material [45, 54] can modify the electron-LO phonon scattering coefficients [53]: This would however affect mostly the quantitative magnitude of the captured charge, and only in a minor way the qualitative features discussed here. In view of chiral optical selection rules and spin splittings, a wave packet initially located in the  $\bar{s} = \bar{v} = 1$  subband can be realized by circularly polarized excitation [42]. Although intervalley scattering mechanisms could in principle transfer charge from  $\mathbf{K}$  to  $\mathbf{K}'$ , the intervalley relaxation time in TMDCs is of several picoseconds in the low temperature limit [55]. In addition, here the spin preserving intervalley transitions are strongly suppressed in view of our excess energy  $E_0$  lying very close to the minimum of the subband with same spin in  $\mathbf{K}'$  (located  $2|\lambda_C|=21$  meV above the minimum of the subband with  $\bar{s} = 1$  in  $\mathbf{K}$ ). Spin-flipping processes induce slow relaxation times of the order of tens of picoseconds at low temperatures [56]. In view of the sub-picosecond time scale considered here (see, e.g., Fig. 3) we thus restrict our attention to one subband. In this work we consider low-density excitations, where the Coulomb-induced scattering is negligible as well [30, 39], such that we do not take the Coulomb interaction into account in our present studies.

## Appendix C: Material parameters

In this work we focus on MoSe<sub>2</sub>, whose above-introduced dispersion relation is given by material parameters  $\lambda_c = -10.5$  meV [57],  $\lambda_v = 90$  meV,  $a_0 \approx 3.3$  Å,  $\Delta_G = 1.47$  eV and  $t = 0.94$  eV [42], resulting in an effective mass of  $m^* = 0.54m_0$  for  $\bar{b} = \bar{s} = \bar{v} = 1$  ( $m_0$  being the free electron mass). Concerning the Fröhlich interaction of Eq. (6), the effective layer thickness  $d$  and  $g_{\text{FR}}$  have been given in [37] for MoS<sub>2</sub>; considering the differences in the material parameters of MoS<sub>2</sub> and MoSe<sub>2</sub> [53], here we use  $d = 5.36$  Å and  $g_{\text{FR}} = 419.7$  meVÅ.

- 
- [1] K. F. Mak, C. Lee, J. Hone, J. Shan and T. F. Heinz, Atomically thin MoS<sub>2</sub>: A new direct-gap semiconductor, Phys. Rev. Lett. **105**, 136805 (2010).  
 [2] A. Splendiani, L. Sun, Y. Zhang, T. Li, J. Kim, C.-Y. Chim, G. Galli and F. Wang, Emerging photolumi-

nescence in monolayer MoS<sub>2</sub>, Nano Lett. **10**, 1271–1275 (2010).

- [3] Q. H. Wang, K. Kalantar-Zadeh, A. Kis, J. N. Coleman and M. S. Strano, Electronics and optoelectronics of two-dimensional transition metal dichalcogenides, Nat. Nan-



- otechnol. **7**, 699–712 (2012).
- [4] A. Kormányos, G. Burkard, M. Gmitra, J. Fabian, V. Zólyomi, N. D. Drummond and V. Fal'ko. *k*·*p* theory for two-dimensional transition metal dichalcogenide semiconductors, *2D Materials* **2**, 022001 (2015).
- [5] A. Branny, G. Wang, S. Kumar, C. Robert, B. Lassagne, X. Marie, B. D. Gerardot and B. Urbaszek, Discrete quantum dot like emitters in monolayer MoSe<sub>2</sub>. Spatial mapping, magneto-optics, and charge tuning, *Appl. Phys. Lett.* **108**, 142101 (2016).
- [6] J. Krustok *et al.*, Optical study of local strain related disordering in CVD-grown MoSe<sub>2</sub> monolayers, *Appl. Phys. Lett.* **109**, 253106 (2016).
- [7] M. Koperski, K. Nogajewski, A. Arora, V. Cherkez, P. Mallet, J.-Y. Veullen, J. Marcus, P. Kossacki and M. Potemski, Single photon emitters in exfoliated WSe<sub>2</sub> structures, *Nat. Nanotechnol.* **10**, 503–506 (2015).
- [8] S. Kumar, A. Kaczmarczyk and B. D. Gerardot, Strain-induced spatial and spectral isolation of quantum emitters in mono- and bilayer WSe<sub>2</sub>. *Nano Lett.* **15**, 7567–7573 (2015).
- [9] Tonndorf, P. *et al.*, Single-photon emission from localized excitons in an atomically thin semiconductor, *Optica* **2**, 347–352 (2015).
- [10] Kern, J. *et al.*, Nanoscale positioning of single-photon emitters in atomically thin WSe<sub>2</sub>, *Adv. Mater.* **28**, 7101–7105, (2016).
- [11] A. Branny, S. Kumar, R. Proux, and B. D. Gerardot, Deterministic strain-induced arrays of quantum emitters in a two-dimensional semiconductor, *Nat. Commun.* **8**, 15053 (2017).
- [12] R. Ferreira and G. Bastard, Phonon-assisted capture and intradot Auger relaxation in quantum dots, *Appl. Phys. Lett.* **74**, 2818–2820 (1999).
- [13] I. Magnusdottir, S. Bischoff, A. V. Uskov, and J. Mørk, Geometry dependence of Auger carrier capture rates into cone-shaped self-assembled quantum dots, *Phys. Rev. B* **67**, 205326 (2003).
- [14] A. Markus and A. Fiore, Modeling carrier dynamics in quantum-dot lasers, *Phys. Status Solidi A* **201**, 338–344 (2004).
- [15] T. R. Nielsen, P. Gartner and F. Jahnke, Many-body theory of carrier capture and relaxation in semiconductor quantum-dot lasers, *Phys. Rev. B* **69**, 235314 (2004).
- [16] J. Seebeck, T. R. Nielsen, P. Gartner and F. Jahnke, Polarons in semiconductor quantum dots and their role in the quantum kinetics of carrier relaxation, *Phys. Rev. B* **71**, 125327 (2005).
- [17] S. Trumm and M. Wesseli, Spin-preserving ultrafast carrier capture and relaxation in InGaAs quantum dots, *Appl. Phys. Lett.* **87**, 153113 (2005).
- [18] A. Mielnik-Pyszczorski, K. Gawarecki and P. Machnikowski, Phonon-assisted tunneling of electrons in a quantum well/quantum dot injection structure, *Phys. Rev. B* **91**, 195421 (2015).
- [19] G. Schedelbeck, W. Wegscheider, M. Bichler and G. Abstreiter, Coupled quantum dots fabricated by cleaved edge overgrowth: From artificial atoms to molecules, *Science* **278**, 1792–1795 (1997).
- [20] Ch. Lienau, V. Emiliani, T. Guenther, F. Intonti, T. Elsaesser, R. Nötzel and K.H. Ploog, Near field optical spectroscopy of confined excitons, *Phys. Status Solidi A* **178**, 471–479 (2000).
- [21] W. Wegscheider, G. Schedelbeck, G. Abstreiter, M. Rother and M. Bichler, Atomically precise GaAs/AlGaAs quantum dots fabricated by twofold cleaved edge overgrowth, *Phys. Rev. Lett.* **79**, 1917–1920 (1997).
- [22] J. A. Brum, and G. Bastard, Resonant carrier capture by semiconductor quantum wells, *Phys. Rev. B* **33**, 1420–1423 (1986).
- [23] T. Kuhn and G. Mahler, Carrier capture in quantum wells and its importance for ambipolar transport, *Solid-state electronics* **32**, 1851–1855 (1989).
- [24] M. Preisel and J. Mørk, Phonon-mediated carrier capture in quantum well lasers, *J. Appl. Phys.* **76**, 1691–1696 (1994).
- [25] D. E. Reiter, E. Y. Sherman, A. Najmaie, and J. E. Sipe, Coherent control of electron propagation and capture in semiconductor heterostructures, *EPL* **88**, 67005 (2009).
- [26] R. Ferreira and G. Bastard, Capture and Relaxation in Self-Assembled Semiconductor Quantum Dots, 2053-2571 (Morgan and Claypool Publishers, San Rafael, 2015).
- [27] F. Lengers, R. Rosati, T. Kuhn, and D. E. Reiter, Spatiotemporal dynamics of carrier capture processes: Simulation of optical signals, *Acta Physica Polonica A* **132**, 372–375 (2017).
- [28] D. Reiter, M. Glanemann, V. M. Axt and T. Kuhn, Controlling the capture dynamics of traveling wave packets into a quantum dot, *Phys. Rev. B* **73**, 125334 (2006).
- [29] D. Reiter, M. Glanemann, V. M. Axt and T. Kuhn Spatiotemporal dynamics in optically excited quantum wire-dot systems: Capture, escape, and wave-front dynamics, *Phys. Rev. B* **75**, 205327 (2007).
- [30] R. Rosati, D. E. Reiter and T. Kuhn, Lindblad approach to spatiotemporal quantum dynamics of phonon-induced carrier capture processes, *Phys. Rev. B* **95**, 165302 (2017).
- [31] R. Rosati, R. C. Iotti, F. Dolcini and F. Rossi, Derivation of nonlinear single-particle equations via many-body lindblad superoperators: A density-matrix approach, *Phys. Rev. B* **90**, 125140 (2014).
- [32] R. Rosati and F. Rossi, Microscopic modeling of scattering quantum non-locality in semiconductor nanostructures, *Appl. Phys. Lett.*, **103**, 113105 (2013).
- [33] R. Rosati and F. Rossi, Scattering nonlocality in quantum charge transport: Application to semiconductor nanostructures, *Phys. Rev. B*, **89**, 205415 (2014).
- [34] R. Rosati, F. Dolcini and F. Rossi, Dispersionless propagation of electron wavepackets in single-walled carbon nanotubes, *Appl. Phys. Lett.*, **106**, 243101 (2015).
- [35] F. Rossi and T. Kuhn, Theory of ultrafast phenomena in photoexcited semiconductors, *Rev. Mod. Phys.* **74**, 895–950 (2002).
- [36] K. Kaasbjerg, K. S. Thygesen and K. W. Jacobsen, Phonon-limited mobility in *n*-type single-layer MoS<sub>2</sub> from first principles, *Phys. Rev. B* **85**, 115317 (2012).
- [37] K. Kaasbjerg, K. S. Bhargavi and S. S. Kubakaddi, Hot-electron cooling by acoustic and optical phonons in monolayers of MoS<sub>2</sub> and other transition-metal dichalcogenides, *Phys. Rev. B* **90**, 165436 (2014).
- [38] D. Taj, R. C. Iotti and F. Rossi, Microscopic modeling of energy relaxation and decoherence in quantum optoelectronic devices at the nanoscale, *Eur. Phys. J. B* **72**, 305–322 (2009).

- [39] M. Glanemann, V. M. Axt, and T. Kuhn, Transport of a wave packet through nanostructures: Quantum kinetics of carrier capture processes, *Phys. Rev. B* **72**, 045354 (2005).
- [40] W.-Y. Shan, H.-Z. Lu and D. Xiao, Spin Hall effect in spin-valley coupled monolayers of transition metal dichalcogenides, *Phys. Rev. B* **88**, 125301 (2013).
- [41] Y. Ferreira, and A. Cortijo, Large conduction band and Fermi velocity spin splitting due to Coulomb interactions in single-layer MoS<sub>2</sub>, *Phys. Rev. B* **90**, 195426 (2014).
- [42] D. Xiao, G.-B. Liu, W. Feng, X. Xu and W. Yao, Coupled spin and valley physics in monolayers of MoS<sub>2</sub> and other group-VI dichalcogenides, *Phys. Rev. Lett.* **108**, 196802 (2012).
- [43] Y. Dinga, Y. Wang, J. Ni, L. Shi, S. Shi and W. Tang, First principles study of structural, vibrational and electronic properties of graphene-like MX<sub>2</sub> (M=Mo, Nb, W, Ta; X=S, Se, Te) monolayers, *Physica B: Condensed Matter* **406**, 2254–2260 (2011).
- [44] Z. Y. Zhu, Y. C. Cheng and U. Schwingenschlögl, Giant spin-orbit-induced spin splitting in two-dimensional transition-metal dichalcogenide semiconductors, *Phys. Rev. B* **84**, 153402 (2011).
- [45] M. M. Ugeda *et al.*, Giant bandgap renormalization and excitonic effects in a monolayer transition metal dichalcogenide semiconductor, *Nat. Mater.* **13**, 1091–1095 (2014).
- [46] G. Berghäuser and E. Malic, Analytical approach to excitonic properties of MoS<sub>2</sub>, *Phys. Rev. B* **89**, 125309 (2014).
- [47] Klots, A. *et al.*, Probing excitonic states in suspended two-dimensional semiconductors by photocurrent spectroscopy, *Scientific reports* **4**, 6608 (2014).
- [48] F. Qu, A. Dias, J. Fu, L. Villegas-Lelovsky and D. L. Azevedo, Tunable spin and valley dependent magneto-optical absorption in molybdenum disulfide quantum dots, *Scientific reports* **7**, 41044 (2017).
- [49] P. Steinleitner, P. Merkl, P. Nagler, J. Mornhinweg, C. Schiller, T. Korn, A. Chernikov and R. Huber, Direct observation of ultrafast exciton formation in a monolayer of WSe<sub>2</sub>, *Nano Lett.* **17**, 1455–1460 (2017).
- [50] K. He, N. Kumar, L. Zhao, Z. Wang, K. F. Mak, H. Zhao and J. Shan, Tightly bound excitons in monolayer WSe<sub>2</sub>, *Phys. Rev. Lett.* **113**, 026803 (2014).
- [51] A. Chernikov, T. C. Berkelbach, H. M. Hill, A. Rigosi, Y. Li, O. B. Aslan, D. R. Reichman, M. S. Hybertsen and T. F. Heinz, Exciton binding energy and nonhydrogenic Rydberg series in monolayer WS<sub>2</sub>, *Phys. Rev. Lett.* **113**, 076802 (2014).
- [52] M. Feierabend, G. Berghäuser, A. Knorr and E. Malic, Proposal for dark exciton based chemical sensors, *Nat. Commun.* **8**, 14776 (2017).
- [53] T. Sohler, M. Calandra, and F. Mauri, Two-dimensional Fröhlich interaction in transition-metal dichalcogenide monolayers: Theoretical modeling and first-principles calculations, *Phys. Rev. B* **94**, 085415 (2016).
- [54] Y. Yu, Y. Yu, C. Xu, Y.-Q. Cai, L. Su, Y. Zhang, Y.-W. Zhang, K. Gundogdu and L. Cao, Engineering substrate interactions for high luminescence efficiency of transition-metal dichalcogenide monolayers, *Adv. Funct. Mater.* **26**, 4733–4739 (2016).
- [55] A. Molina-Sánchez, D. Sangalli, L. Wirtz and A. Marini, Ab initio calculations of ultrashort carrier dynamics in two-dimensional materials: Valley depolarization in single-layer WSe<sub>2</sub>, *Nano Lett.*, **17**, 4549-4555 (2017).
- [56] Y. Song and H. Dery, Transport theory of monolayer transition-metal dichalcogenides through symmetry, *Phys. Rev. Lett.* **111**, 026601 (2013).
- [57] G.-B. Liu, W.-Y. Shan, Y. Yao, W. Yao and D. Xiao, Three-band tight-binding model for monolayers of group-VIB transition metal dichalcogenides, *Phys. Rev. B* **88**, 085433 (2013).